Chemical Engineering Journal 427 (2022) 130949

Contents lists available at ScienceDirect

Chemical Engineering Journal

journal homepage: www.elsevier.com/locate/cej

High-performance quasi-2D perovskite solar cells with power conversion efficiency over 20% fabricated in humidity-controlled ambient air

Xue Lai [a,b,c], Wenhui Li [a], Xiaoyu Gu [a], Hui Chen [c], Yuniu Zhang [a], Gongqiang Li [b,d,*], Ren Zhang [b], Dongyu Fan [a,b], Feng He [c,*], Nan Zheng [e], Jiahao Yu [a], Rui Chen [a], Aung Ko Ko Kyaw [a,*], Xiao Wei Sun [a]

[a] Guangdong University Key Laboratory for Advanced Quantum Dot Displays and Lighting, and Department of Electrical & Electronic Engineering, Southern University of Science and Technology, Shenzhen 518055, PR China
[b] Institute of Advanced Materials (IAM), Nanjing Tech University (NanjingTech), 30 South Puzhu Road, Nanjing 211816, PR China
[c] Shenzhen Grubbs Institute, Department of Chemistry and Guangdong Provincial Key Laboratory of Catalysis, Southern University of Science and Technology, Shenzhen 518055, China
[d] Wuhan National Laboratory for Optoelectronics (WNLO), Huazhong University of Science and Technology (HUST), Luoyu Road 1037, Wuhan, Hubei 430074, PR China
[e] Institute of Polymer Optoelectronic Materials and Devices, State Key Laboratory of Luminescent Materials and Devices, South China University of Technology, Guangzhou 510640, China

ARTICLE INFO

Keywords:
Quasi-2D perovskite
Perovskites solar cells
Humidity-controlled ambient air
3-fluoro-phenylmethyl ammonium (3FBA)

ABSTRACT

Quasi-2D perovskite solar cells (PSCs) have attracted extensive attention recently because of their superior stability to moisture, but their power conversion efficiency (PCE) still lags behind that of 3D counterparts. So, it is urgent to explore more stable and highly efficient quasi-2D PSCs. Herein, we employed fluorinated benzylammonium iodide as bulky cation to fabricate the quasi-2D PSCs. With the bulky action, quasi-2D perovskite films exhibit vertical orientation with less grain boundaries and almost no pinhole, all of which can suppress non-radiative recombination and improve the charge collection in photovoltaic devices. As a result, a remarkable PCE of 20.12% with a relatively high open-voltage circuit of 1.223 V was achieved in champion device. More interestingly, the fabrication of our quasi-2D perovskite was carried out in a humidity-controlled ambient air, which demonstrates much more advantage comparing with other quasi-2D perovskites as the literatures reported so far, in which the preparation of low-dimensional perovskites usually requires a glove box filled with an inert gas. This work shed light on the development of high-quality quasi-2D perovskite film fabricated in humidity-controlled ambient air by simple and easy process, which is appealing for the future industrialization of PSCs with low-cost.

1. Introduction

The past decade has witnessed the rapid growth in organic–inorganic halide perovskite solar cells and the remarkable increase in their power conversion efficiency (PCE), primarily driven by material development, [1–3] understanding on photophysical properties,[4] and device optimization.[5–7] Although the highest PCE has already reached up to 25.5% based on three-dimensional (3D) perovskite solar cells (PSCs),[8] there are still outstanding issues hindering the commercialization of perovskite solar cells, such as environmental stability, photo-stability, ion migration, the low formation enthalpy and the high self-doping effect of 3D perovskites.[9,10] Comparing to the 3D counterparts, quasi-two-dimensional (2D) perovskites with a general formula of $(A)_2(CH_3NH_3)_{n-1}M_nX_{3n+1}$ ($1 \leq n \leq \infty$),[11] exhibit enhanced thermal and moisture stability when they are applied in both photovoltaics and light-emitting diodes [12,13], owing to the incorporation of bulky and hydrophobic organic cations in their structures, which can not only prevent from moisture diffusion into the films, but also enhance the structural stability by forming strong van del Waals interaction between capping organic cations and the [PbI_6] units. [14]

During the last five years, more and more highly efficient quasi-2D PSCs have been reported by incorporating various large organic

* Corresponding authors at: Institute of Advanced Materials (IAM), Nanjing Tech University (NanjingTech), 30 South Puzhu Road, Nanjing 211816, PR China.
E-mail addresses: iamgqli@njtech.edu.cn (G. Li), hef@sustech.edu.cn (F. He), aung@sustech.edu.cn (A.K.K. Kyaw).

https://doi.org/10.1016/j.cej.2021.130949
Received 23 April 2021; Received in revised form 11 June 2021; Accepted 17 June 2021
Available online 21 June 2021

ammonium spacers. For instance, with 4-fluoro-phenylethyl ammonium (4FPEA),[14] 3-bromobenzyl ammonium (3BBA),[15] 2-thiophenemethyl ammonium (ThMA),[16] as organic spacer ligands, the corresponding PSCs show high PCE of 17.3% ($n = 5$), 15.42% ($n = 3$) and 18.20% ($3< n <4$), respectively. Recently, the quasi-2D PSCs based on ThMA has reached a PCE up to 19.06% by employing an assisted crystal growth method.[17] However, the PCEs of quasi-2D PSCs still lag behind that of their 3D counterparts because there are several limitations for quasi-2D perovskite such as high exciton binding energy, large bandgap, quantum confinement effect stemming from quantum-well structure, and poor charge transport across the organic planes.[18] To alleviate the poor charge transport across the organic planes in quasi-2D perovskite, sophisticated crystal growth techniques with judicious control are necessary to form a vertically aligned crystal orientation of quasi-2D perovskite.[19] In general, two main strategies have been developed so far to improve the performance of quasi-2D PSCs. One is to increase the numbers of inorganic layers between two adjacent organic spacers (increase *n*) so that the bandgap and exciton binding energy can be reduced, but this approach sacrifices stability to some extent and usually the enhanced efficiency has thus far been at the cost of stability and vice versa. Another one is to fabricate a 2D/3D hybrid system, in which 2D layer is capping on 3D perovskite as protective layer, [20–22] or 2D perovskite is interspersing between 3D grain.[23,24] With this strategy and additional technique to form graded bandgap at 3D-2D interface, a PCE up to 19.89% has been obtained.[21] Note worthily, although various derivatives of 2D perovskite (2D, quasi-2D and hybrid 2D/3D) exhibit improved stability in air, their fabrication process, including the spin coating and post annealing, requires strictly-controlled condition in a glove box filled with an inert gas to obtain a high-quality film. Therefore, it would be much easier and simpler if we could fabricate these 2D perovskite films with very good reproducibility, phase stability, tolerance in processing parameter fluctuations, and high efficiency in air atmosphere conditions.

It has been known that fluorination of organic materials can improve the efficiency of organic solar cells by optimizing energy levels of the organic materials as well as improving the morphologies of bulk-heterojunction in organic solar cell, [25,26] because the incorporation of fluorine atoms can enhance the intermolecular interaction and improve the hole mobility of an organic molecule.[27] So, it seems a good choice to use fluorinated organic cations as a spacer to enhance the stability and efficiency of PSCs via controlled morphology and good charge transport comparing to its non-fluoro counterpart, which usually inhibits the charge transport in perovskite layer and reduces the efficiency [28,29].

Therefore, employing with 3-fluoro-benzyl ammonium iodide (3FBAI) as the bulky organic cation, herein, we demonstrated a high quality quasi-2D film obtained by appropriate control of crystal growth and post annealing in humidity-controlled ambient air [in air glovebox with relative humidity (RH) ~20% for spin coating step and in open air with RH ~70–90% for annealing step]. The fluorinated quasi-2D perovskite comprises a mixture of multiple phases (different *n* values) with small *n* phases allocated near the substrate, while large *n* phases including 3D phase populated at the top surface. The combined 2D and 3D phases could be achieved by one-step deposition without additional treatments or usage of N_2-filled glovebox, making the fabrication process much easier and simpler. In addition, pinhole-free films with densely packed crystalline grains are formed, even without any grain boundary in most regions of the film. All these facts are beneficial for high-performance quasi-2D PSCs. As a result, the champion device yielded a high PCE of 20.12%, with $J_{SC} = 20.98$ mA cm^{-2}, $V_{OC} = 1.223$ V and FF = 78.41%. The relatively high V_{OC} of 1.223 V is an indicative of high-quality perovskite film and low non-radiative recombination loss. The fabricated devices also exhibited little sensitivity to variation in process parameter (molar ratio of precursors), which is attractive from the manufacturing point of view. In addition, the 3FBAI-based PSC showed a good thermal and humidity stability. The device can maintain 93% of its initial PCE after being heated at 55°C for nearly 1062 h in glove box and can keep 91.5% of its initial PCE after being stored in dark and dry air (RH ~30%) without any encapsulation for nearly 700 h. This work shed light on the development of high-quality quasi-2D perovskite film fabricated in humidity-controlled ambient air by simple and easy process, which is appealing for low-cost manufacturing.

2. Result and discussion

The precursor solution of 3FBAI-based quasi-2D perovskite film was prepared by dissolving 3FBAI (its chemical structure is shown in Fig. S1), methylammonium chloride (MACl) and PbI_2 with a molar ratio of 1.6: 2.5: 3 in N, N-Dimethylformamide (DMF). The precursor solution of 3FBAI-based perovskite was firstly spin-coated on poly[bis(4-phenyl)(2,4,6-trimethylphenyl)amine] (PTAA)-coated ITO glass substrate in air glovebox (RH ~ 20%) and then annealed in open air (RH ~70–90%) for 15 min. The Nuclear Magnetic Resonance (NMR) characterizations of 3FBAI and the Fourier-Transform Infrared (FTIR) Spectrum of the corresponding perovskite films are shown in Fig. S1, Figs. 2 and 3. The additional FTIR peaks of 3FBAI-based perovskite film located at 1262 cm^{-1} is from C-F bond and peaks at 1584, 789, and 690 cm^{-1} is from C-H of benzene, clearly showing the fluorination in the compound.

To evaluate the photovoltaic properties of 3FBAI-based PSCs, we fabricated the device with a planar structure: ITO/PTAA/3FBAI-based PVK/$PC_{61}BM$/BCP/Ag, as shown in Fig. 1a. The energy level of each layer is shown in Fig. 1b, wherein the energy level of quasi-2D perovskite film was calculated from Ultraviolet Photoelectron Spectroscopy (UPS) measurement (Fig. S4), while that of PTAA was referred to previous reports. [30] From UPS measurement, the secondary electron cutoff edges (E_{cutoff}) and the valence regions (E_{onset}) are determined to be 7.0 eV and −8.06 eV, respectively. Using the photon energy of 21.22 eV, the valence band maximum (VBM) of the quasi-2D perovskite film was determined to be −6.16 eV. Since the information depth of UPS is a few nanometers from the surface, the VBM value mainly reflects that of 3D or component with high *n*-values which is populated at top surface (we will discuss it later). Although the VBM of 2D component with small *n*-value cannot be independently measured, similar VBM is expected since that of 2D perovskite shows a negligible variation with *n* values [14]. The Tauc plot (Fig. S5) obtained from UV–vis absorption spectrum revealed that the optical bandgap of the film is 1.59 eV. Since the absorption edge of 2D component is overlapped with that 3D component, the optical bandgap of the film obtained from UV–vis absorption spectrum mainly reflects that of 3D component only, while the actual bandgap of 2D components with small *n* values, which is located near the bottom surface, may have bandgap larger than 1.59 eV. With the bandgap of 1.59 eV at the top surface, the conduction band minimum (CBM) of −4.57 eV is obtained for 3FBAI-based perovskite. Although the CBM of 3FBAI-based perovskite is lower than the lowest unoccupied molecular orbital (LUMO) level of PCBM (-4.3 eV), the electron transport and extraction between the perovskite and PCBM layer are quite effective, which can be proved from photoluminance decay measurement (Fig. S6). Fig. 1c shows the current density–voltage (*J-V*) characteristic of 3FBAI-based device, in which the perovskite film was spin coated and annealed in air condition with RH ~20% and ~70–90%, respectively. As shown in Fig. S7, when the molar ratio of 3FBAI is varied from 1.6 to 2.0, all the devices exhibit very good performance with similar PCEs. The insensitivity of device performance on molar ratio of 3FBAI is desirable from the manufacturing point of view because a slight variation in process parameters due to human or machine error would not influence so much on device performance. The best PCE of 20.12% was obtained from the device based on 3FBAI ratio of 1.6 with $J_{SC} = 20.98$ mA cm^{-2}, $V_{OC} = 1.223$ V and FF = 78.41%. The mean value PCE obtained from 44 fabricated devices is 17.87% with standard deviation of ±1.12% and detailed statistics are shown in Fig. 1d.

Fig. 1e presents the EQE spectra of the champion device based on 3FBAI, and the device exhibits an EQE with plateau of 80% in a broad

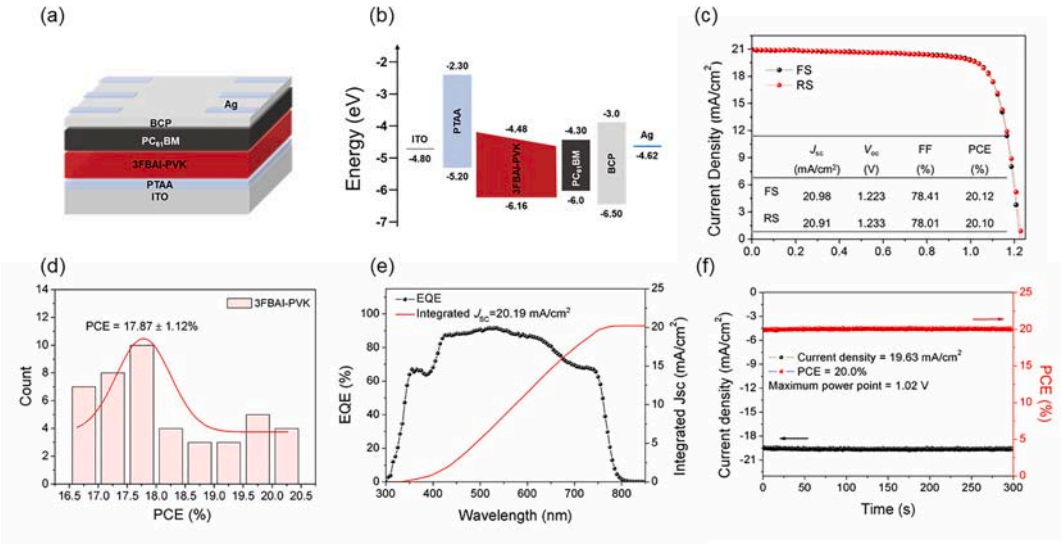

Fig. 1. (a) Device structure, (b) Energy levels of individual layers in the device, (c) *J-V* curves (forward and reverse scans) of the best 3FBAI-based PSCs under AM1.5G illumination, showing negligible hysteresis, (d) PCE statistics of PSCs, (e) EQE spectrum and integrated short-circuit current density, (f) the steady-state efficiency of the champion device at the maximum power point for 300 s.

wavelength range between 415 and 650 nm, and reaches up to 91.57% at 535 nm, suggesting a high photo-to-electron conversion efficiency of the device. A lower EQE beyond 690 nm (<70%) could be attributed to the insufficient light absorption nature of low-dimensional perovskite. The integrated current density calculated from EQE spectrum is about 20.19 mA cm^{-2}, which is only within 3.77% mismatch with the current measured from *J-V* curve. One of the notorious characteristics of perovskite solar cell is hysteresis in *J-V* curve, which is believed to be caused by ion migration to the grain boundaries or perovskite thin-film interfaces, and consequently induces the trap recombination and surface recombination.[31] In order to evaluate the extent of hysteresis, we calculated the hysteresis index (HI) using: $HI = (J_{RS(0.8Voc)} - J_{FS(0.8Voc)})/J_{RS(0.8Voc)}$, where J_{RS}(0.8Voc) and J_{FS}(0.8Voc) are current density at 0.8Voc in reverse and forward scan, respectively.[9,32] The 3FBAI-based device shows an extremely small HI of only 0.0099, indicating a very low bulk and surface recombination in the film, which can be attributed to pinhole-free film with less grain boundaries (we will discuss it later). Furthermore, the steady-state photocurrent density and PCE as a function of time at the maximum power output of 1.02 V were measured for 3FBAI-based device for 300 s as shown in Fig. 1f. A stable and consistent J_{sc} and PCE throughout the test indicates a good stability of the devices under the working condition.

To investigate the influence of 3FBAI on PSC's performance, the quasi-2D perovskite devices based on benzyl ammonium iodide (BAI) (without fluorination) and 3D perovskite devices based on $MAPbI_3$ were fabricated in the same condition (in air with RH ~20% for spin coating and RH ~70–90% for annealing). The best PCEs of devices based-on BAI and $MAPbI_3$ are only 14.39% and 6.40%, respectively (Fig. S8). The performance of various devices obtained from at least 10 devices from each category is summarized in Table 1. The results demonstrate that fluorination of 3FBAI improves device efficiency, especially on J_{sc} (ca. one third improvement comparing to that based on BAI, and almost twice of that based on $MAPbI_3$) due to moisture resistance during fabrication as well as the better charge transport ability and lower bimolecular combination (discuss later). The enhanced moisture resistance of 3FBAI-based perovskite comparing to BAI-based perovskite were further confirmed in contact angel measurement, where water droplets formed a contact angle of 67° on the 3FBAI-based perovskite, which is significantly larger than that on BAI-based film (Fig. S9).

Table 1
Performances of PSCs Based on different active layer fabricated the perovskite film in air condition.

Active layer	scan	Jsc (mA/cm^2)	Voc (V)	FF (%)	Best PCE (%)	Average PCE[a)] (%)
3FBAI-PVK	FS	20.98	1.223	78.41	20.12	17.87±1.12
	RS	20.91	1.233	78.01	20.10	
BAI-PVK	FS	15.73	1.186	76.59	14.29	13.07±0.75
	RS	15.60	1.182	78.01	14.39	
$MAPbI_3$	FS	10.66	0.970	61.89	6.40	5.45±0.95
	RS	10.75	0.979	57.00	6.00	

[a)] The average PCEs was obtained from at least 10 samples

To examine the crystal structure of quasi-2D film compared with 3D film, we measured the X-ray diffraction (XRD) and grazing incidence wide-angle X-ray scattering (GIWAXS) of different perovskite films. As shown in XRD spectrum (Fig. 2a), the $MAPbI_3$ (3D) perovskite exhibits two strong diffraction peaks at 14.08° and 28.44°, which can be assigned to (1 1 0) and (2 2 0) planes of 3D perovskite, respectively. [29] 3FBAI-based perovskite presents two strong peaks at the same 2θ, but different from 3D perovskite, these peaks are attributed to (1 1 1) and (2 0 2) planes of 2D (small *n*) components or (1 1 0) and (2 2 0) planes of 3D components due to the quasi-2D (mixed 2D with 3D) feature. [9,15,29] It has been known that (2 0 2) peak implies the crystallographic planes of 2D perovskite aligning parallel to the substrate due to the perfect vertical orientation of 2D structure while (1 1 1) peak presents the tilted vertical orientation. [9] The dominant (1 1 1) and (2 0 2) peaks in XRD spectra indicates that small *n* components of perovskite are oriented in preferential vertical direction, which is favourable for vertical charge transport in solar cell. [31,33,34] We also found a diffraction peak at lower angle ($2\theta = 5.04°$), which can be assigned to (0 2 0) plane of 2D perovskite with d-spacing of 17.6 Å, [3,9,29] when the 3FBAI-based perovskite film was tested (Fig. S10, Supporting Information). However, no diffraction peak was detected at low angles from the $MAPbI_3$ film, confirming the formation of 2D perovskite in 3FBAI-based film.

GIWAXS patterns of 3FBAI-based film measured at angle of incident $\alpha = 0.2°$ exhibit the strong and discrete Bragg spots, indicating a preferential orientation of perovskite crystals, rather than the diffraction rings or arcs in pure 3D $MAPbI_3$ film which represents the random orientation of crystals (Fig. 2b and c). Some peaks, which indicates the formation of 2D components and highly ordered 2D phase, are clearly observed in 3FBAI-based film. In particular, the peaks at $q = 3.5$ nm^{-1} and 7 nm^{-1} represent the (0 2 0) plane of 2D component, confirming the

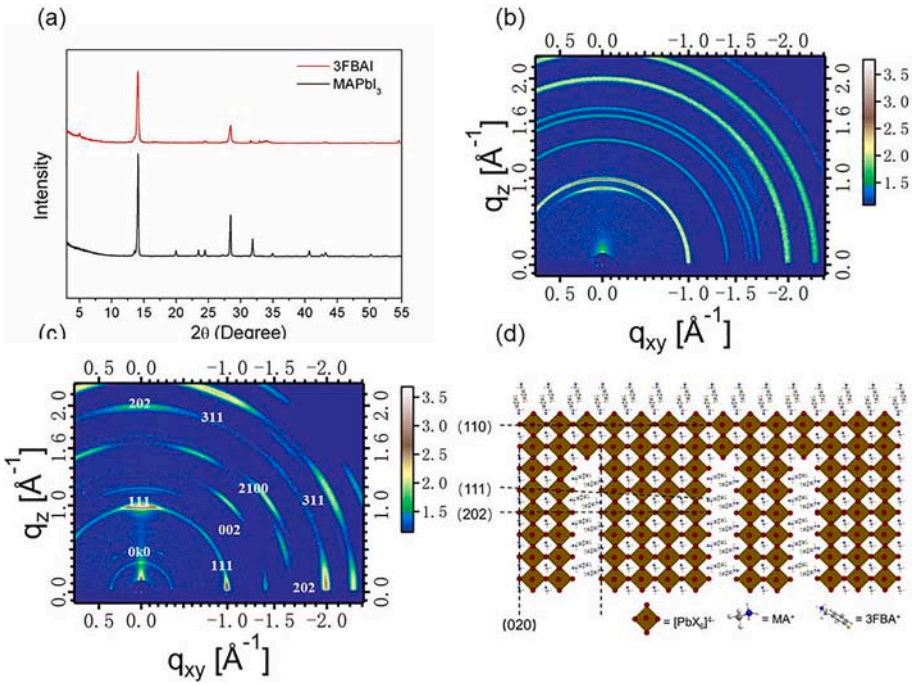

Fig. 2. (a) XRD patterns of control $MAPbI_3$ and 3FBAI-based quais-2D perovskite films. GIWAXS images of (b) control $MAPbI_3$, (c) 3FBAI-based quais-2D perovskite films and (d) the illustration of quais-2D perovskite crystals with 3FBAI as large cation.

formation of highly ordered and periodic layering of small *n* component [9]. In addition, a very strong (1 1 1) plane diffraction peaks located at $q = 10\ nm^{-1}$ and another strong (2 0 2) plane peaks at $q = 20\ nm^{-1}$ along the out-of-plane q_z direction suggest that the quais-2D perovskite crystal grows preferentially along the out-of-plan direction with respect to the substrate, agreeing well with XRD spectrum. The (1 1 1) and (2 0 2) peaks at in-plane q_{xy} direction can be attributed to the titled vertical orientation of 2D crystal. Both XRD and GIWAXS patterns conclude that 2D (small *n*) components are incorporated in 3D component to form quai-2D structure and oriented in vertical direction with a slight tilt. When we tested GIWAXS pattern at low gracing incident angles (0.05° and 0.1°) (Fig. S11), in which X-ray penetrates only top a few nanometers of the film, merely diffraction rings pattern, which is similar to pattern in 3D film, was observed. This suggests that (near) top surface is populated with 3D components or 3FBAI bulky ions, while 2D components with small *n* values are mainly located at the bottom of the film rather than

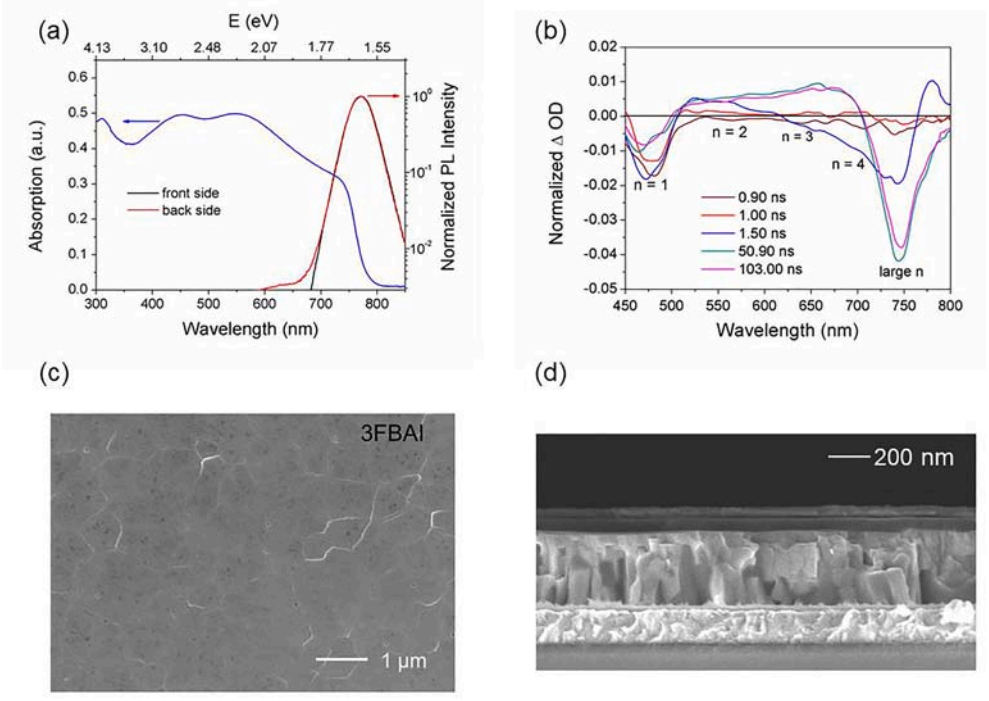

Fig. 3. (a) the absorption and PL spectra (front side and back side excitations) of a quaia-2D perovskite film on quartz substrate. (b) TA spectra for 3FBAI-based perovskite film, the inset number is delay time (ns). (c) SEM image of 3FBAI-based perovskite film and (d) the crossing section of 3FBAI-based device.

top surface.

In general, 2D perovskites comprise the mixture of multiple perovskite phases with different bandgaps (n values) that spontaneously align in the order of n along the normal to the substrate. [9,29] To further investigate compositional phases and their distribution in quasi-2D film, various optical spectroscopy measurements were carried out. Firstly, photoluminescence (PL) spectra of 3FBAI-based perovskite film were collected under the excitation of laser beam at 445 nm from the surface of the film (front excitation) and from the substrate (back excitation). The front excitation of 3FBAI-based perovskite film leads to a Gaussian symmetrical PL peak at ~760 nm contributed from 3D phase of perovskite, whereas the back excitation causes the extra PL emission between 600 nm and 680 nm contributed from small n phases of 2D perovskite (Fig. 3a). The different PL spectra of two configurations of excitation side mean that the lager n values in quasi-2D perovskite are mainly located near the top surface while the small n values are distributed near the substrate, agreeing well with GIWAXS patterns measured at different grazing incident angles. Similar phase distribution was also observed by others. [9]

As shown in Fig. 3a, the UV–vis absorption spectrum displays a peak at 547 nm and 453 nm which can be attributed to the absorption peak of $n = 2$ and $n = 1$ phases, respectively, in addition to the dominant peak at 740 nm stems from 3D phase ($n = \infty$). The various peaks in absorption spectrum also confirms that qausi-2D comprises multiple phases with different n values. To further verify the phase composition in quasi-2D perovskite, femtosecond transient absorption (TA) measurement was also carried out. A pump pulse (325 nm, 1 kHz, 100 fs) was used to excite the perovskite film and the induced absorption changes (△A), as functions of both time and wavelength, were recorded. As shown in Fig. 3b, the TA spectra of quasi-2D film exhibit several photobleaching peaks between 450 nm and 710 nm, which can be assigned to the peaks at small n phases of quasi-2D perovskite, due to the charge carrier filling upon excitation. The bleaching peak at 740 nm represents the 3D phase ($n = \infty$). The photobleaching peaks from TA spectrum are consistent with those in steady-state absorption spectrum (shown in Fig. 3a). The TA spectra of quasi-2D are very similar to that of low-dimensional 2D perovskite film, except that the peak from $n = \infty$ at 740 nm is absent in 2D film (Fig. S12a). In contrast, the TA spectra of $MAPbI_3$ (pure 3D) do not display any photobleaching peaks between 450 nm and 710 nm but exhibit only one strong peak at 740 nm (Fig. S12b). Therefore, TA measurement also confirm the formation of multiple phases in quasi-2D film.

The morphology of perovskite film plays an important role in the device performance through the grain boundaries effect and associated properties such as ion migration and charge carrier recombination and hence, we investigated the film morphology using scanning electron microscopy (SEM). The top SEM image of $MAPbI_3$-film displays the lump-shaped perovskite crystals while that of cross-sectional image exhibits disordered grain accumulation (Fig. S13). In contrast, a full-coverage and pinhole-free film with densely packed micrometer-scale crystalline grains is observed in the top view SEM of 3FBAI-based perovskite film (Fig. 3c). Moreover, the grain boundaries are less apparent compared to those in $MAPbI_3$ film and the grain boundaries even completely disappear in some region, probably due to the passivation of grain boundaries with 3FBAI ions. Less grain boundaries not only suppress the ion migration and charge carrier recombination but also prevent from the moisture penetration into perovskite film, which might be a reason for achieving high PCE of device fabricated in air. In addition, unlike $MAPbI_3$ film, the cross-sectional SEM image of the quasi-2D film reveals that the elongated grains are vertically aligned, exhibiting a vertically oriented growth of the crystals, as observed in XRD and GIWAXS spectra. From the morphology study, we can also clearly see the effect of fluorination in perovskite film. In contract to 3FBAI-based quasi-2D perovskite film, the morphology of BAI-based film exhibits several pinholes and grain boundaries (Fig. S14), implying that fluorination is important for obtaining pinhole-free film with less grain boundaries.

We further investigated the morphology of the films with Atomic Force Microscopy (AFM). The AFM images as shown in Fig. S15, the 3FBAI-perovskite film has a very smooth surface with a root-mean-square roughness (R_{rms}) of 10.504 nm, which is lower than the $MAPbI_3$ film (11.903 nm). From the cross-section SEM of 3FBAI-based device as shown in Fig. 3d, the thickness of perovskite layer is around 350 nm, at which thickness, the light absorption and charge transport are well balanced. To further confirm the electron and hole mobility of quais-2D perovskite film, we measured the dark current–voltage of hole and electron only device by constructing hole-only and electron-only devices, as shown in Fig. S16. The mobility value can be obtained by fitting the SCLC region using Mott-Gurney equation $J = \frac{9}{8}\mu\varepsilon_0\varepsilon_r\frac{V^2}{d^3}$, where J, μ, ε_0, ε_r, V, and d stand for dark current, mobility, the vacuum permittivity, dielectric constant, applied voltage and film thickness, respectively. The 3FBAI-based device has hole mobility of 4.58×10^{-3} $cm^2\ V^{-1}\ s^{-1}$ and electron mobility of 4.69×10^{-3} $cm^2\ V^{-1}\ s^{-1}$, which is quite balanced.

Finally, we discussed the effect of introducing fluorine atoms into the large cations on the active layer and device performance. Generally, the bandgap-voltage offset, $(E_G/q) - V_{OC}$, where q is the elementary charge, is a useful measure to assess the electronic quality of the absorber in a solar cell. [35,36] This offset directly scales with detrimental recombination losses in the device, such as those via deep defects or interfaces. [37] Herein, we used Fourier transform photocurrent spectroscopy (FTPS) to insight into the electronic quality of 3FBAI-based perovskite film. The Urbach energy (E_u) calculated from FTPS can quantify the electronic disorder of 3FBAI-perovskite film. [2] the formula as showing in following:

$$\alpha(E) = \alpha_0[\exp(\frac{E - E_g}{E_U})]$$

where $\alpha(E)$ is the absorption coefficient of the film to photons of different energy, α_0 is a content, E_g is the optical band gap of a semiconductor and the E_U is the urbanch energy. We can take the logarithm of the above formula and then calculate the slope of the tail part of the exponential fitting to get the E_U value. As showing in the semi-log plot of external quantum efficiency (EQE) absorption edge (Fig. 4a), the 3FBAI-based device shows a sharp absorption edge with an E_u 23.24 meV, which is much lower than the BAI-based device (Fig. S17).

Furthermore, the charge recombination in the devices was also qualitatively determined by light intensity-dependent J-V characteristics. Fig. 4b plots the J_{SC} as a function of the incident light intensity (I) and fitted by the power law equation: $J_{SC} \propto I^{\alpha}$. The deviation of ideality factor $\alpha = 1$ indicated the degree of bimolecular recombination. [16,38] Thus, the 3FBAI-based device with $\alpha = 0.96$ suggests the lower bimolecular recombination when we use 3FBAI as large cation for quais-2D perovskite solar cell. In Fig. 4c, a plot of V_{OC} versus the light intensity in logarithmic scale yields a line with the slope mkT/q, where m is the ideality factor, k is the Boltzmann's constant, T is the temperature, and q is an elementary charge. The ideality factor m for BAI- and 3FBAI- based device is 1.65 and 1.26, respectively. This indicates the trap-assisted recombination is greatly suppressed in 3FBAI-based device. Furthermore, the ideally factor (m) calculated from the dark J-V curve of the PSC devices by estimating the slope of the semilogarithmic J-V curve in the diffusion-dominated current region as showing in Fig. S18. Generally, $m = 1$ represents the direct bimolecular recombination while $m = 2$ implies a Shockley–Read–Hall (SRH) recombination dominates, which means indirect recombination by trapping of minority carriers. [39,40] The ideality factor of 3FBAI-based device is 1.42 which is much lower than 1.98 for BAI-based device, indicating that trap-assistant SRH recombination in 3FBAI-based PSC was suppressed. The trend agrees well with the V_{OC} evolution for different illumination intensities (Fig. 4c).

From the dark current plot, we can clearly see that 3FABI-based

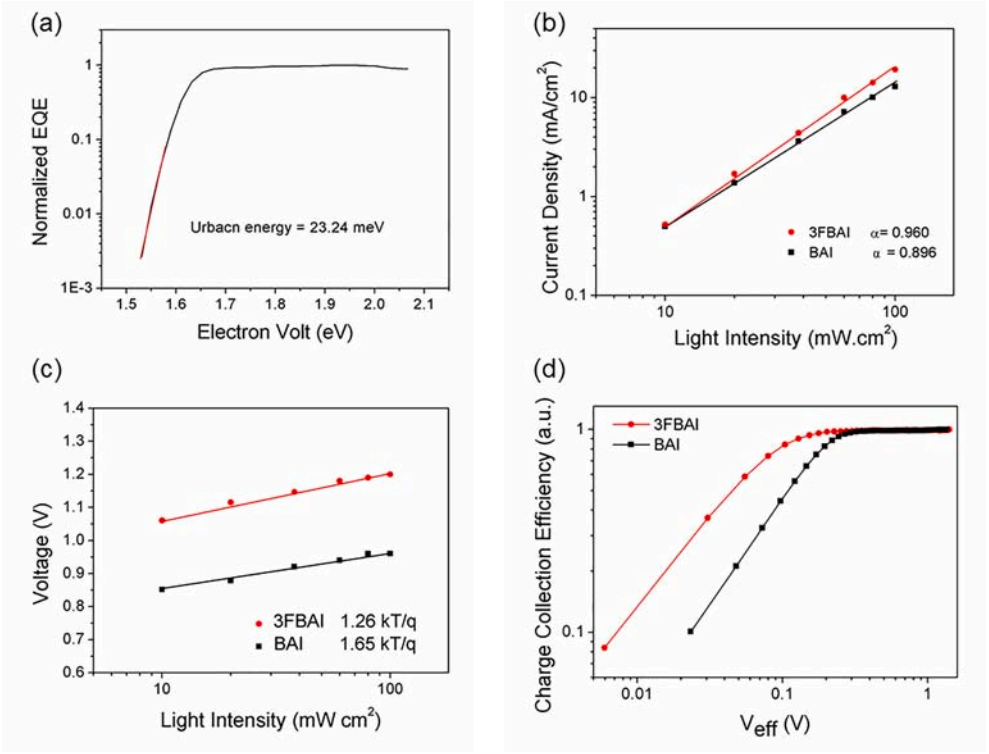

Fig. 4. (a) FTPS spectra of 3FBAI-based perovskite film. (b) J_{SC} values of the photovoltaic devices versus light intensity on a double-logarithmic scale. (c) V_{OC} values of the photovoltaic devices versus light intensity on a seminatural logarithmic scale. (d) Characteristics of charge collection efficiency versus effective voltage (V_{eff}) on a double-logarithmic scale.

device exhibits a low leakage current in negative voltage regime and low positive voltage regime but a high current in high positive voltage regime. This indicates a high shunt resistance (R_{SH}) and a low series resistance (R_S) in the device, which agrees well with R_S and R_{SH} calculated from the *J-V* curve under illumination. The R_S of 3FBAI-based PSC is 2.69 Ω.cm^2 that is lower than that of BAI-based device (5.92 Ω.cm^2) and pure 3D-based device (17.22 Ω.cm^2). (Note: the series resistances of the devices are calculated from the slope of dV/dI around V_{oc}). The R_{SH} of 3FBAI-based device is 2305.89 Ω.cm^2, while the R_{SH} of BAI- and pure 3D-based devices show only 1176.37 and 1618.75 Ω.cm^2, respectively (Note: R_{SH} = calculate the slope of dV/dI in *J-V* curve around J_{sc}). The higher R_{SH} reduces the leakage current and hence improves FF.

To understand charge collection behavior in the photovoltaic devices, the photocurrent density (J_{ph}) versus effective voltage (V_{eff}) measurement were further conducted (Fig. 4d). J_{ph} is calculated as $J_{ph} = J_L - J_D$, where J_L and J_D are the current density under illumination and in the dark, respectively. V_{eff} is determined by $V_{bi} - V_{app}$, where V_{bi} is the built-in voltage which refers to the voltage at which $J_{ph} = 0$ and V_{app} is the applied bias voltage. The charge collection efficiency (η_c), taking both the charge transport in the perovskite and transfer at interface into account, could be characterized by the ratio of $J_{ph}/J_{ph,sat}$ under different V_{eff}, where $J_{ph,sat}$ is the saturated photocurrent under high V_{eff} (2 V or more), where internal electric field is so high that all the photogenerated carriers are swept out to the electrode without recombination, and hence limited only by the absorbed photons. [41–43] η_c of 3FBAI-based device is higher than that of BAI-based device under any V_{eff}. Quantitively, η_c of 3FBAI- and BAI-based devices are 0.997 and 0.972, respectively, under short circuit condition, suggesting the better charge transport and collection in 3FBAI-based device. This finding supports our initial concept that the charge transport in the perovskite film can be improved by fluorination in organic cations through enhanced molecular interaction. In addition, fluorination in organic cations results in pinhole-free film and less grain boundaries, consequently, the non-radiative recombination loss (both trap-assisted recombination and bimolecular recombination) are suppressed and a high V_{oc} of 1.223 V is achieved in photovoltaic devices.

The long-term stability of devices based on 3D perovskite $MAPbI_3$ and 3FBAI-based quais-2D perovskite aged by temperature and humidity were further investigated. The thermal stability test on the devices at 55°C in glove box shows that 3FBAI-based device has better thermal stability than $MAPbI_3$-based device; the former maintains 93% of its initial PCE, whereas the latter drops to 31.5% of its initial PCE after 672 h (Fig. 5a). Similarly, 3FBAI-based device exhibits a better moisture stability than MAPbI3-based device does. After being stored in ambient condition (RH = 35%) in dark for 792 h, the unencapsulated 3FBAI-based quasi-2D devices retain average 91.5% of their original efficiency, while the pure 3D-based devices drop to 72.5% of its initial efficiency. The better moisture stability of 3FBAI-based device can be attributed to the improved film quality with pinhole-free and less grain boundaries and moisture-resistance nature of fluorinated large organic cations.

3. Conclusion

In summary, we demonstrated a highly efficient quasi-2D PSCs by employing 3FBAI as the large cation to fabricate quasi-2D perovskite film in humidity-controlled ambient air. The quasi-2D perovskite comprises mixture of vertically oriented multiple phases with small *n* values located at the bottom and large *n* values populated at the top surface. The pinhole-free perovskite film with densely packed micrometer-size crystalline grains and less grain boundaries leads to good charge transport with balanced electron and hole mobility, low charge carrier recombination, excellent moisture resistance and air stability. The champion device exhibited a PCE of 20.12% with J_{SC} = 20.98 mA cm^{-2}, V_{OC} = 1.223 V and FF = 78.41%. This work sheds light on the importance of fluorinated large cations to fabricate high-quality quasi-2D perovskite film under ambient condition for highly efficient and air-stable perovskite solar cells and other optoelectronic devices.

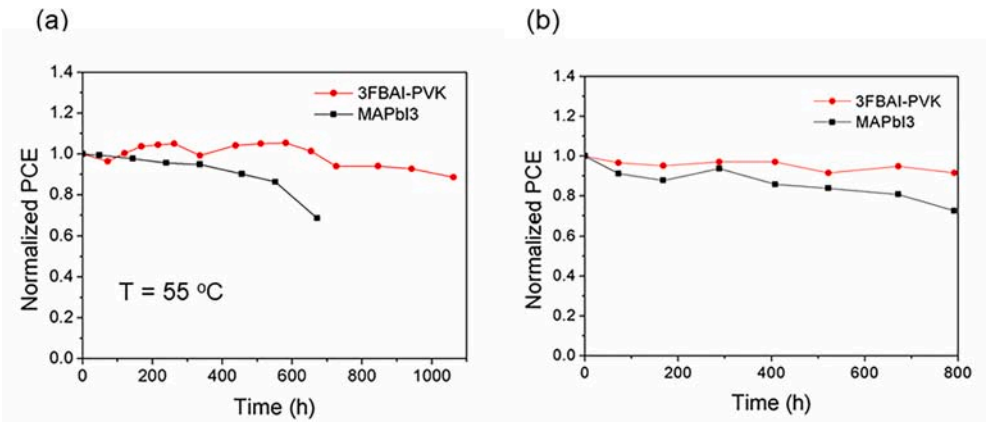

Fig. 5. (a) Normalized PCE versus time for unencapsulated devices stores in N_2 at 55°C for 1062 h. (b) Normalized PCEs versus time for unencapsulated devices stored in ambient condition (RT, RH around 30%) for 672 h.

Declaration of Competing Interest

The authors declare that they have no known competing financial interests or personal relationships that could have appeared to influence the work reported in this paper.

Acknowledgments

Prof. A. K. K. Kyaw thanks for general support by Guangdong Basic and Applied Basic Research Foundation (No. 2020A1515010916), Guangdong University Key Laboratory for Advanced Quantum Dot Displays and Lighting (No. 2017KSYS007), and High-level University Fund (No. G02236004).

Prof. G. Li thanks for the general supported by the National Key R&D Program of China (No. 2017YFA0204704), the National Natural Science Foundation of China (Nos. 51773091, 22075140, 61604069), Nature Science Foundation of Jiangsu Province (No. BK20171465) and the Open Project Program of Wuhan National Laboratory for Optoelectronics No. 2020WNLOKF010.

Prof. F. He thanks the financial support from Guangdong Provincial Key Laboratory of Catalysis (No. 2020B121201002), Guangdong Innovative and Entrepreneurial Research Team Program (No. 2016ZT06G587) and Shenzhen Sci-Tech Fund (No. KYTDPT20181011104007).

Authors would like to acknowledge Prof Jianpu Wang for his discussion in this work and invaluable suggestions to manuscript.

Appendix A. Supplementary data

Supplementary data to this article can be found online at https://doi.org/10.1016/j.cej.2021.130949.

References

[1] H. Zhu, Y. Liu, F.T. Eickemeyer, L. Pan, D. Ren, M.A. Ruiz-Preciado, B. Carlsen, B. Yang, X. Dong, Z. Wang, H. Liu, S. Wang, S.M. Zakeeruddin, A. Hagfeldt, M. I. Dar, X. Li, M. Gratzel, Tailored Amphiphilic Molecular Mitigators for Stable Perovskite Solar Cells with 23.5% Efficiency, Adv. Mater. 32 (2020) 1907757.

[2] M. Jeong, I.W. Choi, E.M. Go, Y. Cho, M. Kim, B. Lee, S. Jeong, Y. Jo, H.W. Choi, J. Lee, J.-H. Bae, S.K. Kwak, D.S. Kim, C. Yang, Stable perovskite solar cells with efficiency exceeding 24.8% and 0.3-V voltage loss, Science 369 (6511) (2020) 1615–1620.

[3] Z. Hu, G. Tang, J. Miao, T. Fu, T. Li, Q. Tai, H. Meng, F. Yan, π-Extended Spiro Core-Based Nonfullerene Electron-Transporting Material for High-Performance Perovskite Solar Cells, Adv. Funct. Mater. 30 (2020) 2001073.

[4] J. Li, B. Pradhan, S. Gaur, J. Thomas, Predictions and Strategies Learned from Machine Learning to Develop High-Performing Perovskite Solar Cells, Adv. Energy Mater. 9 (2019) 1901891.

[5] X. Zhu, M. Du, J. Feng, H. Wang, Z. Xu, L. Wang, S. Zuo, C. Wang, Z. Wang, C. Zhang, X. Ren, S. Priya, D. Yang, S.(. Liu, High-efficiency perovskite solar cells with imidazolium-based ionic liquid for surface passivation and charge transport, Angew. Chem. Int. Ed. 60 (8) (2021) 4238–4244.

[6] F. Gao, Y. Zhao, X. Zhang, J. You, Recent Progresses on Defect Passivation toward Efficient Perovskite Solar Cells, Adv. Energy Mater. 10 (2020) 1902650.

[7] J.-H. Im, I.-H. Jang, N. Pellet, M. Grätzel, N.-G. Park, Growth of CH3NH3PbI3 cuboids with controlled size for high-efficiency perovskite solar cells, Nat. Nanotechnol 9 (11) (2014) 927–932.

[8] https://www.nrel.gov/pv/assets/pdfs/best-research-cell-efficiencies.20200925.pdf.

[9] J. Shi, Y. Gao, X. Gao, Y. Zhang, J. Zhang, X. Jing, M. Shao, Fluorinated Low-Dimensional Ruddlesden-Popper Perovskite Solar Cells with over 17% Power Conversion Efficiency and Improved Stability, Adv. Mater. 31 (2019) 1901673.

[10] H. Chen, Y. Xia, B.o. Wu, F. Liu, T. Niu, L. Chao, G. Xing, T. Sum, Y. Chen, W. Huang, Critical role of chloride in organic ammonium spacer on the performance of Low-dimensional Ruddlesden-Popper perovskite solar cells, Nano Energy 56 (2019) 373–381.

[11] P. Gao, A.R. Bin Mohd Yusoff, M.K. Nazeeruddin, Dimensionality engineering of hybrid halide perovskite light absorbers, Nat. Commun. 9 (2018) 5028.

[12] W. Fu, H. Liu, X. Shi, L. Zuo, X. Li, A.K.Y. Jen, Tailoring the Functionality of Organic Spacer Cations for Efficient and Stable Quasi-2D Perovskite Solar Cells, Adv. Funct. Mater. 29 (2019) 1900221.

[13] N. Wang, L. Cheng, R. Ge, S. Zhang, Y. Miao, W. Zou, C. Yi, Y. Sun, Y. Cao, R. Yang, Y. Wei, Q. Guo, Y. Ke, M. Yu, Y. Jin, Y. Liu, Q. Ding, D. Di, L. Yang, G. Xing, H. Tian, C. Jin, F. Gao, R.H. Friend, J. Wang, W. Huang, Perovskite light-emitting diodes based on solution-processed self-organized multiple quantum wells, Nat. Photonics 10 (11) (2016) 699–704.

[14] L.N. Quan, M. Yuan, R. Comin, O. Voznyy, E.M. Beauregard, S. Hoogland, A. Buin, A.R. Kirmani, K. Zhao, A. Amassian, D.H. Kim, E.H. Sargent, Ligand-Stabilized Reduced-Dimensionality Perovskites, J. Am. Chem. Soc. 138 (8) (2016) 2649–2655.

[15] R. Yang, R. Li, Y. Cao, Y. Wei, Y. Miao, W.L. Tan, X. Jiao, H. Chen, L. Zhang, Q. Chen, H. Zhang, W. Zou, Y. Wang, M. Yang, C. Yi, N. Wang, F. Gao, C. R. McNeill, T. Qin, J. Wang, W. Huang, Oriented Quasi-2D Perovskites for High Performance Optoelectronic Devices, Adv. Mater. 30 (2018) 1804771.

[16] H. Lai, B. Kan, T. Liu, N. Zheng, Z. Xie, T. Zhou, X. Wan, X. Zhang, Y. Liu, Y. Chen, Two-Dimensional Ruddlesden-Popper Perovskite with Nanorod-like Morphology for Solar Cells with Efficiency Exceeding 15, J. Am. Chem. Soc. 140 (37) (2018) 11639–11646.

[17] H. Lai, D. Lu, Z. Xu, N. Zheng, Z. Xie, Y. Liu, Organic-Salt-Assisted Crystal Growth and Orientation of Quasi-2D Ruddlesden-Popper Perovskites for Solar Cells with Efficiency over 19, Adv. Mater. 32 (2020) 2001470.

[18] H. Tsai, R. Asadpour, J.C. Blancon, C.C. Stoumpos, J. Even, P.M. Ajayan, M. G. Kanatzidis, M.A. Alam, A.D. Mohite, W. Nie, Design principles for electronic charge transport in solution-processed vertically stacked 2D perovskite quantum wells, Nat. Commun. 9 (2018) 2130.

[19] Z. Wang, Q. Wei, X. Liu, L. Liu, X. Tang, J. Guo, S. Ren, G. Xing, D. Zhao, Y. Zheng, Spacer Cation Tuning Enables Vertically Oriented and Graded Quasi-2D Perovskites for Efficient Solar Cells, Adv. Funct. Mater. 31 (5) (2021) 2008404, https://doi.org/10.1002/adfm.v31.510.1002/adfm.202008404.

[20] Y. Hu, J. Schlipf, M. Wussler, M.L. Petrus, W. Jaegermann, T. Bein, P. Müller-Buschbaum, P. Docampo, Hybrid Perovskite/Perovskite Heterojunction Solar Cells, ACS Nano 10 (6) (2016) 5999–6007.

[21] Y. Bai, S. Xiao, C. Hu, T. Zhang, X. Meng, H. Lin, Y. Yang, S. Yang, Dimensional Engineering of a Graded 3D–2D Halide Perovskite Interface Enables Ultrahigh Voc Enhanced Stability in the p-i-n Photovoltaics, Adv. Energy Mater. 7 (2017) 1701038.

[22] G. Grancini, C. Roldan-Carmona, I. Zimmermann, E. Mosconi, X. Lee, D. Martineau, S. Narbey, F. Oswald, F. De Angelis, M. Graetzel, M.K. Nazeeruddin, One-Year stable perovskite solar cells by 2D/3D interface engineering, Nat. Commun. 8 (2017) 15684.

[23] J. Lu, L. Jiang, W. Li, F. Li, N.K. Pai, A.D. Scully, C.M. Tsai, U. Bach, A.N. Simonov, Y.B. Cheng, L. Spiccia, Diammonium and Monoammonium Mixed-Organic-Cation Perovskites for High Performance Solar Cells with Improved Stability, Adv. Energy Mater. 7 (2017) 1700444.
[24] Z. Wang, Q. Lin, F.P. Chmiel, N. Sakai, L.M. Herz, H.J. Snaith, Efficient ambient-air-stable solar cells with 2D–3D heterostructured butylammonium-caesium-formamidinium lead halide perovskites, Nat. Energy 2 (2017) 17135.
[25] X. Li, J. Yao, I. Angunawela, C. Sun, L. Xue, A. Liebman-Pelaez, C. Zhu, C. Yang, Z. G. Zhang, H. Ade, Y. Li, Improvement of Photovoltaic Performance of Polymer Solar Cells by Rational Molecular Optimization of Organic Molecule Acceptors, Adv. Energy Mater. 8 (2018) 1800815.
[26] S. Dai, F. Zhao, Q. Zhang, T.-K. Lau, T. Li, K. Liu, Q. Ling, C. Wang, X. Lu, W. You, X. Zhan, Fused Nonacyclic Electron Acceptors for Efficient Polymer Solar Cells, J. Am. Chem. Soc. 139 (3) (2017) 1336–1343.
[27] Y. Yang, K. Wang, G. Li, X. Ran, X. Song, N. Gasparini, Q.Q. Zhang, X. Lai, X. Guo, F. Meng, M. Du, W. Huang, D. Baran, Fluorination Triggered New Small Molecule Donor Materials for Efficient As-Cast Organic Solar Cells, Small 14 (2018) 1801542.
[28] I.C. Smith, E.T. Hoke, D. Solis-Ibarra, M.D. McGehee, H.I. Karunadasa, A layered hybrid perovskite solar-cell absorber with enhanced moisture stability, Angew. Chem. Int. Ed. 53 (42) (2014) 11232–11235.
[29] D.H. Cao, C.C. Stoumpos, O.K. Farha, J.T. Hupp, M.G. Kanatzidis, 2D Homologous Perovskites as Light-Absorbing Materials for Solar Cell Applications, J. Am. Chem. Soc. 137 (24) (2015) 7843–7850.
[30] R. Li, C. Yi, R. Ge, W. Zou, L. Cheng, N. Wang, J. Wang, W. Huang, Room-temperature electroluminescence from two-dimensional lead halide perovskites, Appl. Phys. Lett. 109 (2016), 151101.
[31] C.M.M. Soe, W. Nie, C.C. Stoumpos, H. Tsai, J.C. Blancon, F. Liu, J. Even, T. J. Marks, A.D. Mohite, M.G. Kanatzidis, Understanding Film Formation Morphology and Orientation in High Member 2D Ruddlesden-Popper Perovskites for High-Efficiency Solar Cells, Adv. Energy Mater. 8 (2018) 1700979.
[32] H.S. Kim, N.G. Park, Parameters Affecting I-V Hysteresis of CH3NH3PbI3 Perovskite Solar Cells: Effects of Perovskite Crystal Size and Mesoporous TiO2 Layer, J. Phys. Chem. Lett. 5 (2014) 2927–2934.
[33] G. Wu, X. Li, J. Zhou, J. Zhang, X. Zhang, X. Leng, P. Wang, M. Chen, D. Zhang, K. Zhao, S.F. Liu, H. Zhou, Y. Zhang, Fine Multi-Phase Alignments in 2D Perovskite Solar Cells with Efficiency over 17% via Slow Post-Annealing, Adv. Mater. 31 (2019) 1903889.
[34] H. Tsai, W. Nie, J.-C. Blancon, C.C. Stoumpos, R. Asadpour, B. Harutyunyan, A. J. Neukirch, R. Verduzco, J.J. Crochet, S. Tretiak, L. Pedesseau, J. Even, M. A. Alam, G. Gupta, J. Lou, P.M. Ajayan, M.J. Bedzyk, M.G. Kanatzidis, A.D. Mohite, High-efficiency two-dimensional Ruddlesden-Popper perovskite solar cells, Nature 536 (7616) (2016) 312–316.
[35] T. Tiedje, E. Yablonovitch, G.D. Cody, B.G. Brooks, Limiting Efficiency of Silicon Solar Cells, IEEE Trans. Electron Devices 31 (5) (1984) 711–716.
[36] R.R. King, D. Bhusari, A. Boca, D. Larrabee, X.Q. Liu, W. Hong, C.M. Fetzer, D. C. Law, N.H. Karam, Band gap-voltage offset and energy production in next-generation multijunction solar cells, Prog. Photovoltaics Res. Appl. 19 (2011) 797–812.
[37] S. De Wolf, J. Holovsky, S.J. Moon, P. Loper, B. Niesen, M. Ledinsky, F.J. Haug, J. H. Yum, C. Ballif, Organometallic Halide Perovskites: Sharp Optical Absorption Edge and Its Relation to Photovoltaic Performance, J. Phys. Chem. Lett. 5 (2014) 1035–1039.
[38] A.K.K. Kyaw, D.H. Wang, C. Luo, Y. Cao, T.Q. Nguyen, G.C. Bazan, A.J. Heeger, Effects of Solvent Additives on Morphology, Charge Generation, Transport, and Recombination in Solution-Processed Small-Molecule Solar Cells, Adv. Energy Mater. 4 (2014) 1301469.
[39] T. He, S. Li, Y. Jiang, C. Qin, M. Cui, L. Qiao, H. Xu, J. Yang, R. Long, H. Wang, M. Yuan, Reduced-dimensional perovskite photovoltaics with homogeneous energy landscape, Nat. Commun. 11 (2020) 1672.
[40] S. Xiong, Z. Hou, S. Zou, X. Lu, J. Yang, T. Hao, Z. Zhou, J. Xu, Y. Zeng, W. Xiao, W. Dong, D. Li, X. Wang, Z. Hu, L. Sun, Y. Wu, X. Liu, L. Ding, Z. Sun, M. Fahlman, Q. Bao, Direct Observation on p- to n-Type Transformation of Perovskite Surface Region during Defect Passivation Driving High Photovoltaic Efficiency, Joule 5 (2) (2021) 467–480.
[41] A.K.K. Kyaw, D.H. Wang, D. Wynands, J. Zhang, T.-Q. Nguyen, G.C. Bazan, A. J. Heeger, Improved light harvesting and improved efficiency by insertion of an optical spacer (ZnO) in solution-processed small-molecule solar cells, Nano Lett. 13 (8) (2013) 3796–3801.
[42] P.W.M. Blom, V.D. Mihailetchi, L.J.A. Koster, D.E. Markov, Device Physics of Polymer: Fullerene Bulk Heterojunction Solar Cells, Adv. Mater. 19 (2007) 1551–1566.
[43] T. Zhou, H. Lai, T. Liu, D. Lu, X. Wan, X. Zhang, Y. Liu, Y. Chen, Highly Efficient and Stable Solar Cells Based on Crystalline Oriented 2D/3D Hybrid Perovskite, Adv. Mater. 31 (2019) 1901242.